High Q THz photonic crystal cavity on a low loss suspended Silicon platform

Elias Akiki, Marc Faucher, Mathias Vanwolleghem, Mattias Verstuyft, Bart Kuyken, Benjamin Walter, Jean-Francois Lampin, Guillaume Ducournau

High Q THz photonic crystal cavity on a low loss suspended Silicon platform

Elias Akiki, Mattias Verstuyft, Bart Kuyken, Benjamin Walter, Marc Faucher, Jean-François Lampin, Guillaume Ducournau, Mathias Vanwolleghem.

***Abstract*— In this work, we present an ultra-high Q cavity at Terahertz (THz) frequencies. The designed cavity is built on a low loss suspended silicon (Si) waveguide. The substrate removal under the waveguide and the use of optimized deep reactive ion etching processing is the main reason for observing very low losses of this design $\alpha < 0.09$ dB/mm. This very low loss behavior of this designed platform is also demonstrated by the measurement of a 1D photonic wire crystal cavity with Q>18000. Different cavity layouts are adjusted in order to maximize the transmittance while maintaining high Q. A design with reduced number of etched crystal holes achieve a Q>1500 and high transmittance T>70%. These structures are presented at sub-mm waves (around 600GHz) for the design of a gas sensor in this frequency region, but the principles can be scaled and redesigned for other frequencies in the THz band.**

***Index Terms*—THz waveguide, THz photonic crystal cavity, high resistivity Silicon, Quality factor, propagation losses.**

I. Introduction

Terahertz waves (0.3-10 THz) are the electromagnetic (EM) waves that fall between the upper edge of electronics and lower edge of photonics in the EM spectrum. These waves offer a variety of applications in different domains. Their non-ionizing property, low energy and capability of penetrating different types of materials, including some opaque ones in the visible range, make them helpful for medicine, biosensors and imaging [1],[2]. The presence of rotational resonances of many polar molecules in this frequency region allow THz waves to act as a unique spectroscopic tool[3],[4]. For many of these applications, the availability of efficient passive and active THz components (sources, detectors, waveguides, resonators, …), is essential.

Manuscript received April 16, 2020; revised July 17, 2020; accepted August 14, 2020. Date of publication XXXX. This study was undertaken as part of the Terafood project, which is financially supported by the European Regional Development Fund and the province Oost-Vlaanderen (INTERREG V FR-WA-VL 1.1.11).

E. Akiki, M. Faucher, J-F. Lampin, G. Ducournau and M. Vanwolleghem are with Institute of Electronics Microelectronics and Nanotechnology (IEMN), CNRS, University of Lille, 59650 Villeneuve d'Ascq, France (e-mail: Elias.akiki@univ-lille.fr).

M. Verstuyft and B. Kuyken are with Photonics Research Group Department of Information Technology, Ghent University-imec, 9052 Ghent, Belgium.

B. Walter and M. Faucher are with Vmicro SAS, 59650 Villeneuve d'Ascq, France.

In integrated circuits low-loss waveguides are essential to transmit the EM waves between all passive and active components of a circuit and to ensure the transition from off- to on-chip. Different types of guides have been reported at THz frequencies. Metallic waveguides (MWG) with scaled dimensions similar as those used in the microwave and millimeter wave bands have been among the first reported. Despite the different fabrication techniques proposed to fabricate such integrated waveguides, they still suffer from surface roughness, high metallic losses and complicated assembly process [5]–[7]. While MWG are limited by size and ohmic losses, dielectric waveguides may be fabricated by waferscale foundry techniques and may be easier to integrate. Several types of dielectric waveguides have been reported, such as ridge waveguides and line defect photonic crystal (PhC) waveguides [8]–[11]. At THz frequencies the available material systems that combine high index, transparency and planar processing are limited. High resistivity silicon (HR-Si) is the most used material, due to its very low absorption coefficient and large non-dispersive refractive index [12],[13]. Silicon on glass waveguides presented in [8], use the refractive index contrast between Si and glass which are bonded together in order to create the guiding channel for mm-waves. The extracted propagation loss of this design correspond to 0.063, 0.028 and 0.053 dB/mm, for 55-65, 90-110 and 140-170 GHz bands. At frequencies beyond 400 GHz, the absorption of the glass substrate material increases dramatically [13], [14] and it becomes useless for guiding purposes. To avoid material losses, [9] proposes a layout where the glass is locally etched and the guiding layer is suspended by Si supporting beams (SB). A loss average of 0.054 dB/mm over 440-550 GHz frequency band is reported for this suspended waveguide. The process is laborious and the large number of SB increases the scattering losses due to roughness at the SB edges, adding to that a bonding of HR-Si/Glass followed by glass etching steps are still required. The line defect PhC with 0.4 dB/mm of average losses over 540-630 GHz, reported by [10], suffers likewise from increased scattering losses due to the large number of etched holes. The one reported in [15] covers a very short frequency band region 326-331 GHz with low losses below 0.01 dB/mm, while outside this band, losses are much higher. In this work we present the design, fabrication and characterization of a fully suspended HR-Si waveguide, that requires wafer processing with only two steps and no bonding. The advantage of this design is that it uses an air cladding without presence of any other lossy material. Only few anchors are used in order to have a mechanically stable structure and to limit the scattering losses.

This article has been accepted for publication in a future issue of this journal, but has not been fully edited. Content may change prior to final publication. Citation information: DOI 10.1109/TTHZ.2020.3019928, IEEE Transactions on Terahertz Science and Technology

Besides analyzing the loss mechanisms in this purely index guided novel integrated THz waveguide, one-dimensional PhC wire waveguides have also been fabricated and measured. A scheme to confine the air band mode of such a PhC cavity in an air hole cavity by apodization of the PhC period is experimentally demonstrated. Such cavities have been commonly demonstrated in the visible, near and mid-infrared (midIR) [16]–[23]. At THz frequencies a similar design for 100 and 200 GHz frequencies with Q= 11900 and 2200 respectively was demonstrated by [24]. Aside from [24], 1D photonic crystal cavities were very little investigated in the THz region. Other dielectric cavities such as ring resonators and 2D PhC cavities with high quality factors up to 15000 have been reported [25]–[31]. With respect to all these achievements, this work reports a similarly high quality factor (Q≈18000) but with the resonant energy mainly confined in a PhC air hole. In this work we designed and measured a high-Q 1D PhC THz cavity, by etching a crystal of air holes in the suspended core of the membrane wire waveguide taking advantage of its low losses. The designed cavity allows to confine THz EM waves at frequencies around 630-650 GHz in a strongly subwavelength air hole of a 1D wire PhC cavity. Achieving such a confinement in air at these frequencies, where many absorption peaks of different molecules belong, can have a huge potential for THz sensing or strong coupling applications.

In section II of this paper we present the numerical results and the design of the proposed waveguide, followed in section III by the design of the taper that ensures the low insertion losses caused by the transition from MWG of the source to the designed Si waveguide. Section IV treats the design of the PhC cavity. Finally, in V and VI, the fabrication process and the experimental measurements results of both designs are presented respectively.

II. Waveguide Design

The designed THz waveguide is based on index guiding between two materials with high refractive index contrast. HR-Si is a perfect candidate for the core material of the waveguide due to its large, and frequency independent (nondispersive) refractive index ($n_{Si=}$ 3.42) at Terahertz (THz) frequencies [12], [13]. High resistivity float zone (HRFZ) silicon represents very low losses at THz frequencies. While such core material is considered as loss-less, cladding materials with a sufficiently lower refractive index than Si such as silica, borosilicate, crystal quartz or other Glasses have important absorption losses that moreover increase dramatically at frequencies beyond 500 GHz [13], [14]. An ideal THz guide thus consists of HRFZ-Si guiding channel surrounded by air. The high refractive index contrast between Si and air defined as $\Delta = \frac{n_1^2 - n_2^2}{2n_1^2} = 45\%$ [32], allows to strongly confine modes with respect to the guiding channel dimensions. Lumerical FDTD and Lumerical mode solver [33] are used to simulate the modal analysis of the device. For an infinite width waveguide the maximal thickness allowing a single mode guiding is given by $T = \frac{\lambda_0}{2\sqrt{n_2^2 - n_1^2}} \approx 76\,\mu m$ (at 650GHz). For finite width waveguide, mode propagation constants are numerically analyzed at several widths and thicknesses using a numerical sweep.

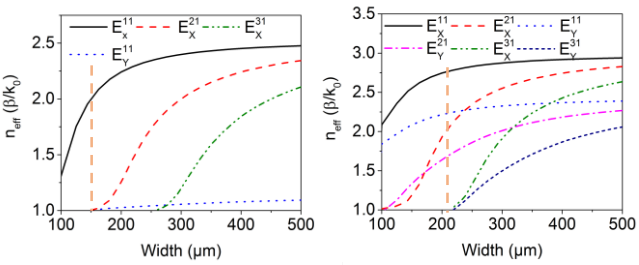

Fig. 1 Normalized propagation constant at 650 GHz as function of waveguide width (W) for a) thickness T=50 µm and b) T=90 µm. The dashed vertical orange line represents the chosen widths.

Figure 1 represents the modes propagation constant at 650 GHz, as function of waveguide width for two particular thicknesses. As represented in figure 1.a by the orange dashed vertical line, a width (W) of 150 µm and a thickness (T) of 50 µm represents the dimensions of a single mode waveguide. This waveguide has a monomode behavior at 500-650 GHz (fig 2.a), but it disadvantages arise in the low mode confinement inside Silicon (58%) (fig 3.a). As our interest goes out to design a PhC cavity for sensing applications [34]–[36] a multimode waveguide with high confinement factor is desired. The designed channel has a width (W) and thickness (T) of 210x90 µm. With such dimensions the waveguide allows to highly confine the fundamental mode E_x^{11} inside the core (89%) (fig. 3.b), while the propagation of the second symmetric mode E_x^{31} remains prevented (fig. 1.b). This waveguide is quadrimodal, with guided, $E_x^{11}, E_y^{11}, E_x^{21}, E_y^{21}$-modes in the frequency band 500-650 GHz (fig. 2.b).

In order to suspend this structure, anchors are designed to hold the guiding channel with two supporting silicon structures on the sides (fig.4). The dimensions of the anchors are defined after studying their impacts on the mode perturbation and propagation losses.

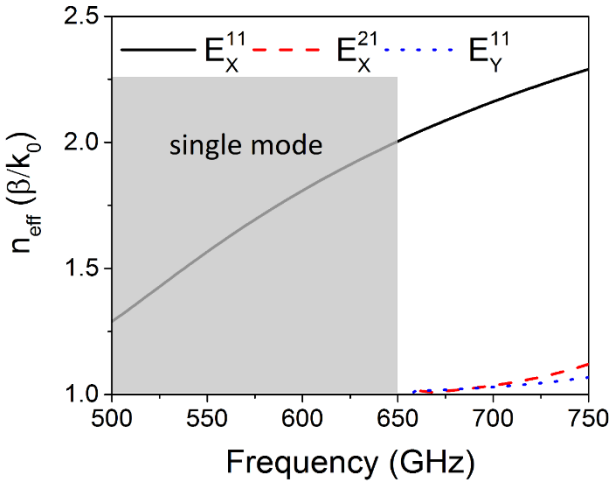

This article has been accepted for publication in a future issue of this journal, but has not been fully edited. Content may change prior to final publication. Citation information: DOI 10.1109/TTHZ.2020.3019928, IEEE Transactions on Terahertz Science and Technology

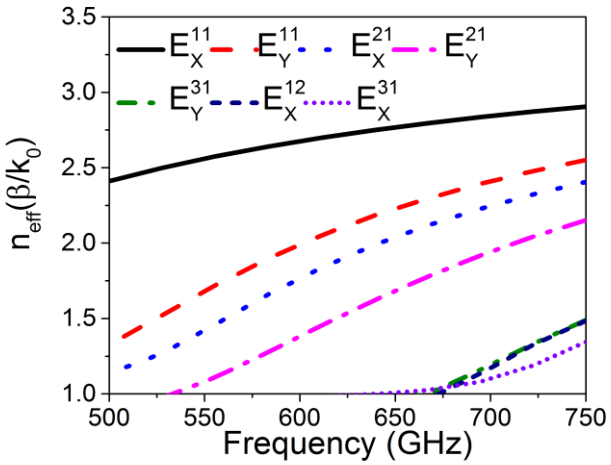

(b)

Fig. 2 Normalized propagation constant (β/k0) of the suspednded waveguide with: a) W=150µm T=70µm and b) W=210µm T=90µm

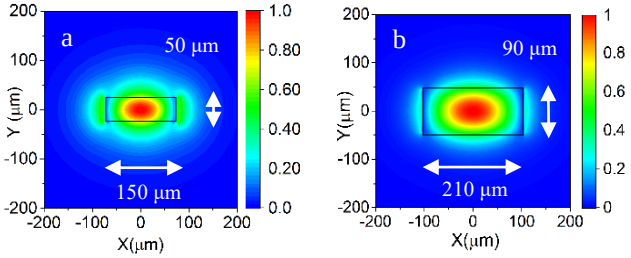

Fig. 3. Normalized E_x cross section of the fundamental mode at 650 GHz for a) single mode structure W=150 µm T=70µm and b) multimode structure W=210 µm T=90 µm

The higher order modes of odd symmetry (E_x^{21},E_y^{21}) will in principle not be excited upon symmetric injection (see Section III), while the fundamental TM-like mode E_y^{11} will, due to its lower effective index, radiate when we will consider the Bloch modes in a PhC layout. Moreover, a TE-like excitation will not couple to this mode.

Figure 5 represents the simulated losses per pair of anchors for different anchors width. All simulations are done first using the real refractive index of HR-Si, i.e. without taking material losses into account. In order to estimate anchor losses in Lumerical FDTD we launched the fundamental waveguide mode and monitored its power loss over a certain waveguide length containing 4 pairs of anchors, sufficiently spaced apart (1.5 mm) preventing any collective effect. The simulation window is closed by PML (Perfect Matched Layer) boundaries to prevent spurious numerical interface reflections. With no anchors, using these numerical conditions, losses are absent. The represented losses are therefore purely due to scattering at the anchors. The simulation results confirm that the impact of the anchors decreases with their width.

In order to maintain a compromise between mechanical stability and low scattering loss the dimensions of the anchors are chosen to be 20x300x90 µm (see fig. 4.c). The lateral dimension is chosen so as to avoid any spurious leakage to the Si layer of the supporting wafer to which the anchors are attached (see fig. 4.a).

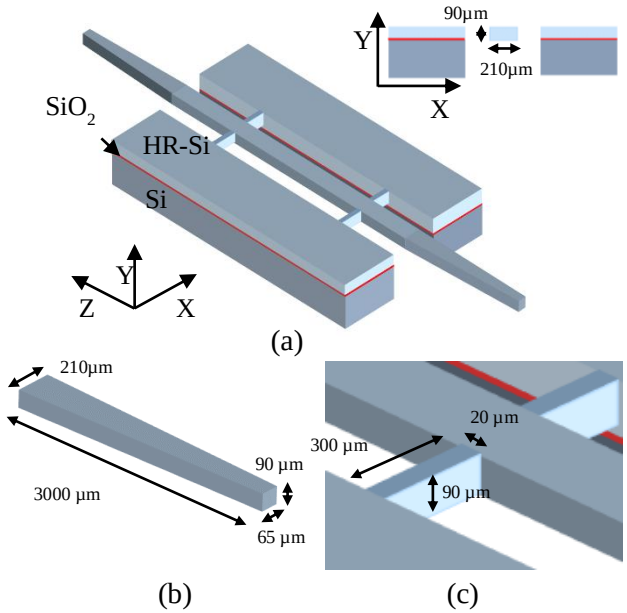

Fig. 4. a) Suspended waveguide inset: transversal cross section of the waveguide b) Taper dimensions c) supporting anchors dimensions

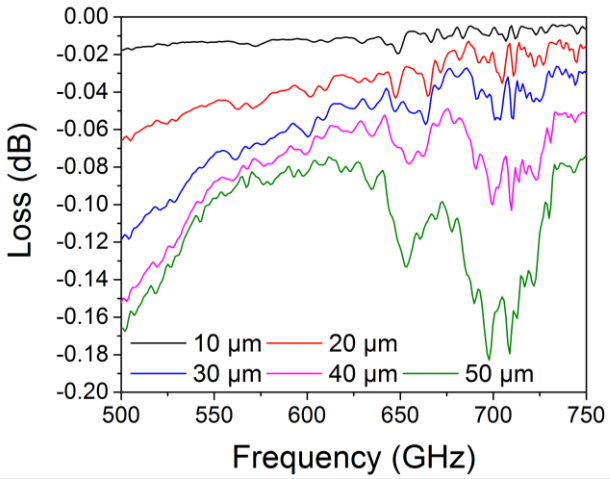

Fig. 5. Simulated loss per anchor pair for different anchor size

III. Taper Design and Insertion Losses

To characterize the designed waveguide, S-parameter measurements are done using a vectorial network analyzer (VNA) coupled to frequency extenders (VNAX) with MWG WR-1.5 ports in the frequency range 500-750 GHz. In order to achieve smooth injection and good transition from MWG ports to the silicon waveguide, adiabatic tapers are added at the in- and output sides of the suspended waveguide. Wave impedance is represented by [37]

$$Z_{MWG}=\frac{\eta_0}{\sqrt{1-\left(\frac{f_c}{f}\right)^2}} \quad (1)$$

for an air filled MWG and,

$$Z_{Si} = \frac{\eta_0}{\sqrt{\epsilon_{eff}}} \quad (2)$$

for Si waveguide. With $\eta_0 = \sqrt{\frac{\mu_0}{\epsilon_0}}$ the free space impedance, f_c the MWG cutoff frequency which is $f_c = 393\ GHz$ for WR-1.5 MWG, f working frequency and $\epsilon_{eff} = n_{eff}^2$ effective permittivity of the propagating mode inside Si waveguide. To reduce the mismatch between these two impedances, the Si taper edge should be small enough, in order for the fundamental mode to still be guided but weakly confined in the Si with lowest n_{eff}. A taper edge section of 65x90 µm, slightly confines the fundamental mode with an $n_{eff} = 1.03$ at 650 GHz and therefore represent the smallest impedance mismatch with guided wave inside MWG, before E_x^{11} goes to cut-off (see fig. 6). A larger section leads to stronger Si confinement, resulting in a higher effective index and therefore deeper reflection dips especially at higher frequencies. Once the mode at the taper edge is excited, a gentle variation of the taper dimension is necessary to prevent that the fundamental mode couples to higher order radiative or guided modes, before reaching the Si waveguide. For that, the taper length L_t has to be much longer than the beat length L_b corresponding to the coupling length between the fundamental mode and the second symmetric mode.

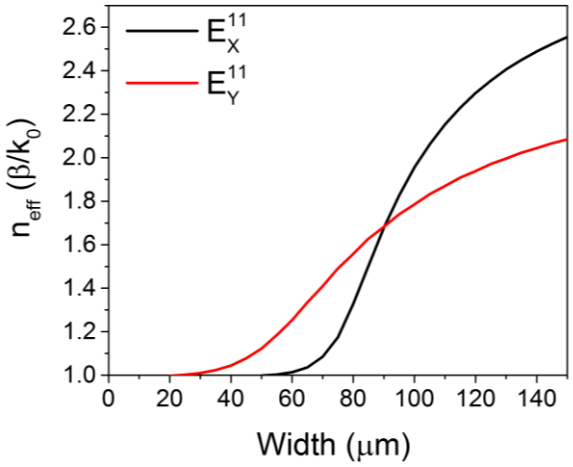

Fig. 6. Normalized propagation constant function of taper width variation

L_b and L_t are defined by [38]

$$L_b = \frac{2\pi}{\beta_1 - \beta_2} \quad (3)$$

$$L_t = \frac{\Delta W}{2\tan^{-1}\theta} \quad (4)$$

where $\beta_1 = n_{eff1}k_0$ and $\beta_2 = n_{eff2}k_0$ are the propagation constant of the two first symmetric modes, where $k_0 = \frac{2\pi}{\lambda_0}$ is the free space propagation constant. $\Delta W = W_1 - W_2$ =145 µm, width difference between taper edges and θ taper's variation angle. So according to the adiabaticity criterion the variation angle θ has to be smaller than θ_{min}

$$\theta \ll \theta_{min} = \frac{\Delta W(\beta_1 - \beta_2)}{4\pi} \quad (5).$$

In our design the long side of the waveguide is tapered and reduced down to 65 µm over a length of 3000 µm, while the short side corresponding to the thickness of the waveguide, remains 90 µm (fig. 4.b). This slow variation with a very small angle of 0.048 rad << θ_{min}, allows an adiabatic transition of modes, and prevents any energy exchange with higher order guided or radiative modes. The taper designed is long enough to conserve the fundamental guided mode. Longer tapers with 4000 µm and smallest slope angle 0.036 rad, have almost the same performance.

In a MWG the electric field $\vec{E}$ of the fundamental mode is oriented along the short side of the waveguide, while in the dielectric one $\vec{E}$ is oriented along the long side. In order to have the best overlap between these two modes the MWG is rotated by 90°. The numerical aperture of such a waveguide at 500 GHz is N.A.=0.79 and 0.53 at 750 GHz so a strong diffraction occurs at the output of this MWG especially at lower frequencies (ie 500GHz). Placing the taper outside the MWG, presents high coupling losses. To estimate the insertion and return losses caused by the transition of EM wave from the MWG to the Si waveguide through the taper, a FDTD simulation has been done. The simulated structure is composed of two metallic waveguides (WR-1.5) of 191x381 µm air guiding channel, surrounded by a PEC (perfect electrical conductor) layer to form the metallic boundaries, and 2 Si (n_{Si}=3.42) tapers in between. For several depths of insertion of the taper inside the MWG (starting at perfect butt-coupling 0mm), the simulated insertion (S_{21}) and return (S_{11}) loss are represented in figure 7 and 8. In figure 7 the taper is considered to be perfectly centered at the MWG ports, and the effect of its position inside the MWG along the propagation direction (Z) is presented. For different positions of taper the return losses are below -10 dB (below the red dashed line) except for perfect butt coupling, which confirms the low impedance mismatch. However, the best coupling and the lowest insertion loss is achieved for the positions where the taper is well inserted inside the MWG. For positions below 1mm, the taper cross section at the output of MWG does not exceed 100x90µm. For these dimensions the fundamental mode at low frequencies is slightly confined with low $n_{eff} = 1.1$ at 500 GHz, which increases the insertion loss due to the coupling with radiative modes. Insertion losses are very low (0.15 dB at 600 GHz), for positions above 1mm.

The simulated results of insertion losses show also some oscillations that correspond to a Fabry-Pérot cavity effect, between the two MWG ports with a free spectral range ~10-15GHz, corresponding to a cavity effect of about 5mm for an effective index of ~2.5. This precisely twice the taper length (corrected with the insertions). The low ripple reconfirms the strong coupling. In figure 9 the magnitude of $\vec{E}$ at the transition between the MWG and the taper is represented for three different frequencies at 1mm insertion well centered inside. The large radiative field part at 500 GHz correspond to the high insertion losses represented in figure 7 at low frequencies. Experimentally, it is not easy to be perfectly aligned, so it is important to study the effect of misalignment. Figure 8 represent the insertion losses, for a X and Y off axis displacement and rotation. A Y displacement perpendicularly to $\vec{E}$ direction (X direction) doesn't show big effect on the insertion and return losses, while a misalignment in the

This article has been accepted for publication in a future issue of this journal, but has not been fully edited. Content may change prior to final publication. Citation information: DOI 10.1109/TTHZ.2020.3019928, IEEE Transactions on Terahertz Science and Technology

direction of $\vec{E}$ or an angular deviation breaks the modal symmetry, and some dips appears in S_{21} at certain frequencies where the higher order anti-symmetric mode is excited, while S_{11} remains low. In conclusion, the designed taper, allows to feed the Si waveguide, from WR-1.5 MWG ports with very low losses.

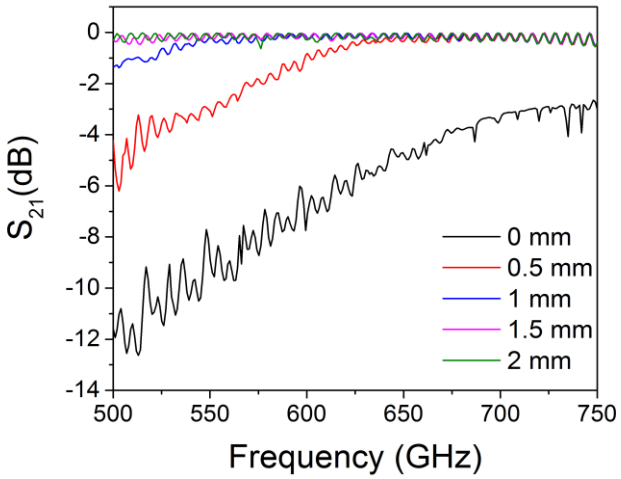

(a)

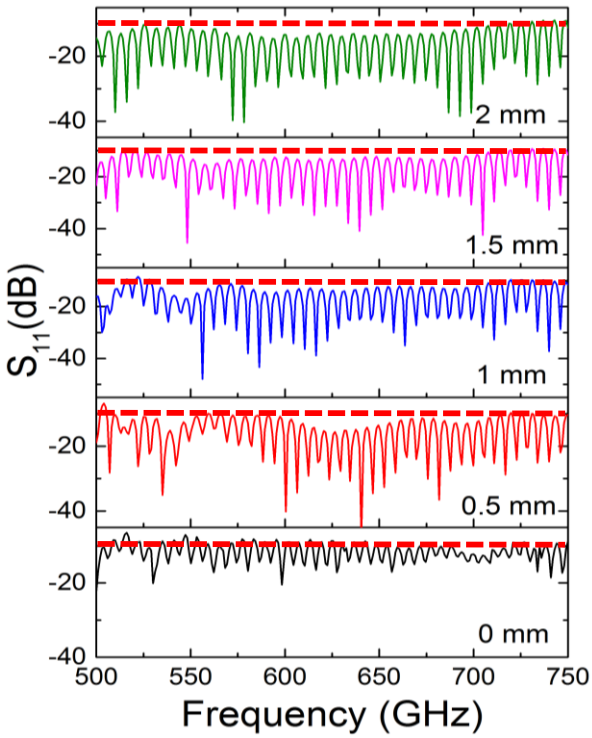

(b)

Fig. 7. Simulated insertion losses for different position of taper inside MWG with the red dashed horizontal line indicating the 10 dB level a) S_{21} parameter (transmittance) b) S_{11} parameter (Reflectance)

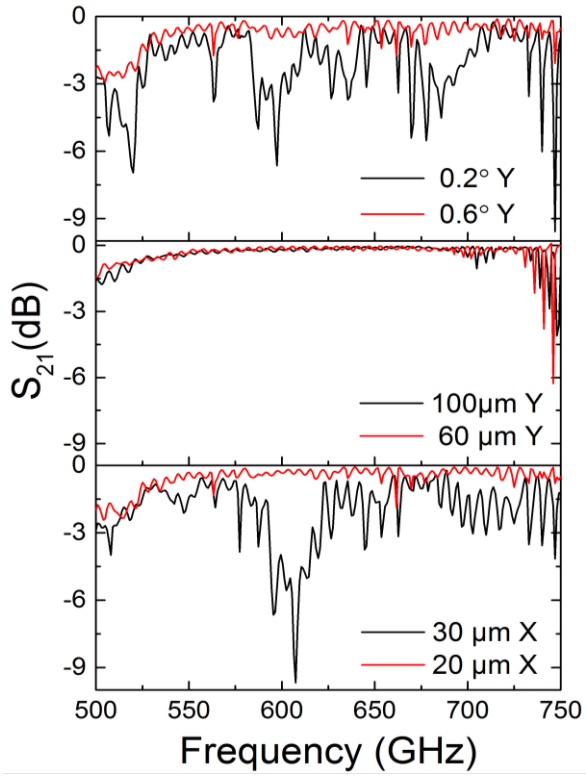

(a)

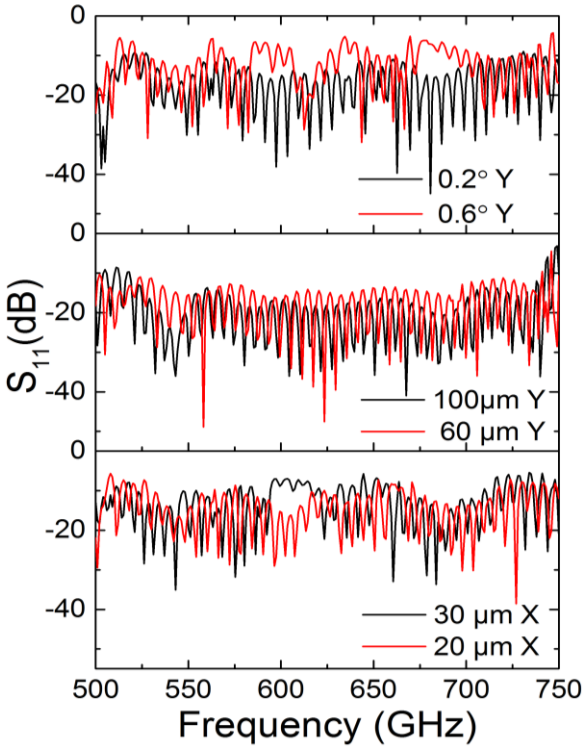

(b)

Fig. 8. Simulated insertion losses for different misaligned position of taper at 1 mm inside MWG a) S21 parameter (transmittance) b) S11 parameter (Reflectance)

This article has been accepted for publication in a future issue of this journal, but has not been fully edited. Content may change prior to final publication. Citation information: DOI 10.1109/TTHZ.2020.3019928, IEEE Transactions on Terahertz Science and Technology

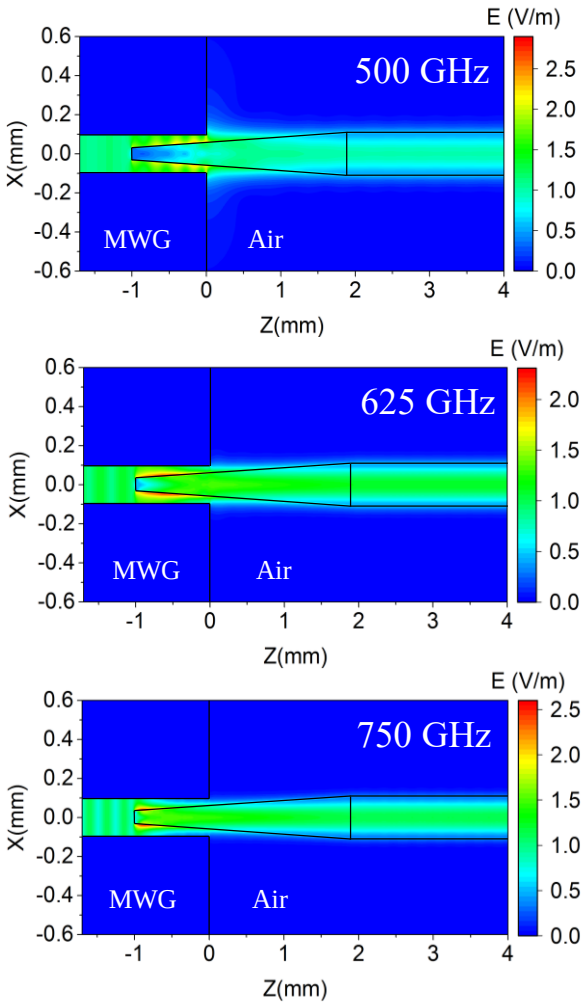

Fig. 9. Electric field transition from MWG to the dielectric waveguide taper at 3 different frequencies 500, 625 and 750 GHz

IV. PHOTONIC CRYSTAL CAVITY DESIGN

This novel integrated THz waveguide platform has been subsequently investigated to serve as a building block for deep subwavelength confinement of THz energy by creating a 1D PhC wire cavity. The design consists in creating a defect mode inside a photonic bandgap similar to nanocavities presented in the NIR [16], [20], [21], [39], [40]. The bandgap and its central frequency is adjusted by choosing the proper etching period and hole radius. In this design, to simplify the fabrication process, we choose to vary the period between holes in order to create the defect mode. However, any other variation that breaks the periodicity such as changing the radius of the holes or the width of the waveguide, could also create a defect mode. Using Comsol Multiphyscis [41], the Bloch modal dispersion of two 1D photonic crystals wires with 29 µm etching radius and two different etching periods (a_1=106.56 µm and a_2=120.65 µm) are calculated and represented in figure 10. These particular periods, represent a large band gap (100 GHz), around 600 GHz. This frequency is chosen for the sake of the specific molecular gas sensing that we are developing this platform for [4]. The design presented here can be rescaled to any reasonable THz frequency. By increasing the period, the band gap shifts toward lower frequencies, which is obviously in rough approximation to be understood by the Bragg condition $\lambda = 2n_{Beff}a$ with $\lambda = \frac{c}{f}$ Bloch mode wavelength, n_{Beff} Bloch mode effective index and a the etching period. For gas sensing purposes our design aims at achieving maximal confinement in the etched air holes (fig.11.b). In other words, the designed cavity needs to trap an air Bloch mode (upper band in fig.10, AM in fig.11.a). In view of the above, this can be achieved by apodizing the crystal periodicity with an increasing step towards to the cavity center, thereby effectively pulling down the air band into the band gap.

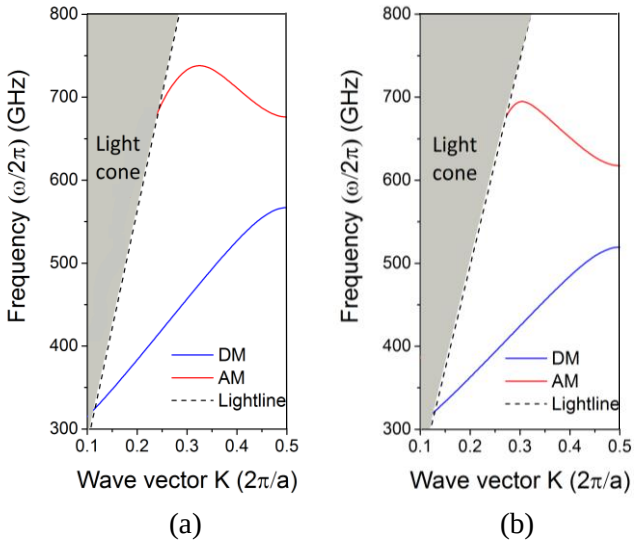

Fig. 10. Band diagram of two photonic crystals with different period a) a=106.56µm and b) a=120.65 µm

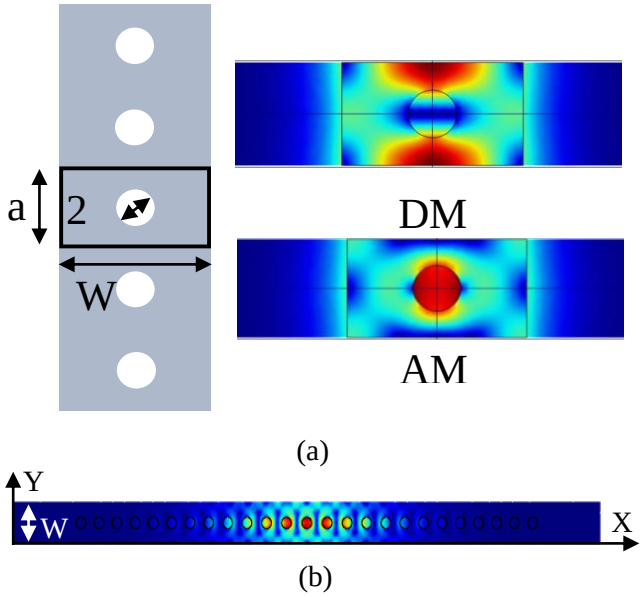

Fig. 11. Normalized electric field of dielectric and air mode for one period of the PhC structure in (a), and normalized electric field of the cavity fundamental resonant mode in (b)

The precise apodization profile of the period from 106.56 µm to 120.65 µm will be detailed below. On the other hand, a cavity with a dielectric resonant mode could be designed in the

opposite way by reducing the etching period instead of increasing it.Two main loss sources are present in such a cavity type. The in-plane losses, due to the mode losses in the waveguide, and the out-of-plane losses related to coupling to radiative modes. The quality factor $Q = \frac{\omega_0 \tau}{2}$ is the dimensionless representation of losses, which is defined by the photon lifetime τ at a frequency $f_0 = \frac{\omega_0}{2\pi}$ inside the cavity. It is important to design a cavity with high Q factor, corresponding to longer photon cavity lifetimes therefore increased molecular interaction time and ultimately an increased sensitivity for sensing applications. The total quality factor Q can be split into its two contributing loss mechanisms Q_w for waveguide losses (in-plane losses) and Q_r for radiative losses (out-of-plane losses) with

$$\frac{1}{Q} = \frac{1}{Q_r} + \frac{1}{Q_w} \quad (6)$$

The in-plane losses are governed by mirror strength (reflectivity), and material loss which depends on material conductivity. Mirror strength is governed by the number of etched holes. In our design we chose N=25 holes. This number of holes is sufficient to increase the reflectivity to 90%. Having a perfect mirror, is a way to increase Q_w, but this also reduces the transmission of the defect mode (it is perfectly reflected). For a photoacoustic sensing application [34]–[36] which this cavity is designed for, the transmission is not so important. In other applications, such as sensing by direct absorption measurements, transmission is much more important. We therefore also considered the possibility to adjust the design in order to increase the transmission, while maintaining a reasonable Q. The same cavity with a lower number of etched holes (N=21 and N=17 resp.) are also measured experimentally. The designed structure is not only adjusted to minimize the in-plane, but also to minimize the out-of-plane losses in order to achieve the highest possible Q factor. One way to have low radiative losses is already achieved by having the structure fully suspended in air as described before. The absence of a substrate reduces radiative losses, by pulling up the light cone to be far away from the Brillouin-zone edge [42],[23]. Similarly, in [17] the period (distance between holes) is parabolically apodized. This parabolical change, allows to obtain a Gaussian envelope of the electromagnetic field decay. The Fourier transform of such an envelope contains less k-components inside the light cone (leaky region) [17]. So finally the period variation is represented by the function below (7).

$$P_i = P_c + (P_m - P_c)\left(\frac{i}{11}\right)^2 \quad (7)$$

With P_m the starting period (106.56) µm and P_c the central period where the air defect mode is confined (120.65µm). P_i represents the varying period between holes with i going from 0 to 11, for a total of 12 periods at both sides of the central hole (giving a total of 25 holes). After defining the parameters of our structure, we performed a 3D simulation using Lumerical FDTD, to calculate and optimize the resonance frequency and its quality factor. The Q-factor depends also on the material absorption coefficient used in the calculation. For high resistivity silicon (ρ=10 kΩ.cm) the material which we are using, absorption losses are reported in [12], [13] to be less than 0.01 cm^{-1} at frequencies below 1 THz. Thus in the calculations n_{Si}=3.42 is used as material refractive index with κ_{Si}= 3 x 10^{-5} for the material absorption coefficient. After making a convergence test, the numerical results present a resonance frequency at 636 GHz with a $Q = 3 \times 10^4$. Such a high Q-factor for air confined PhC cavities at THz frequencies has never been reported. In order to put this in perspective, rescaling this to the NIR region would (at equal photon lifetimes) imply a cavity with Q up to 10^7, or in other words among the strongest reported. As mentioned before this design can be rescaled to other THz frequencies by judiciously varying the geometrical parameters.

V. Fabrication process

The waveguide fabrication process consists of two etching steps. A high resistivity SOI (Silicon on insulator) wafer (ρ > 10kΩ.cm), is composed of 90µm of HR-Si, on top of 300 µm of low resistivity silicon with 2 µm of SiO_2 in between. The device layer is the guiding channel, which requires one lateral etching to define the waveguide's core. The different fabrication steps are represented in figure 12. The wire guide, its anchors and the PhC crystal holes are etched in a single deep reactive ion etching step (DRIE) with the buried oxide layer as etch stop layer. We used a switched SF_6/C_4F_8 plasma process where etching alternates with passivation, enabling to reach 90 µm depth with a 5 µm resist mask, allowing very good lateral definition for the tiny anchor beams [43]. Moreover, we optimized this process by using fast switching, which enables to reduce the sidewall roughness down to the range 30nm-60 nm. Similar backside processing is then performed to define the suspended structures (supported by the anchor beams). Once the guiding channel is etched from the top and the back, a final step of HF etching allows to remove the SiO_2 layer.

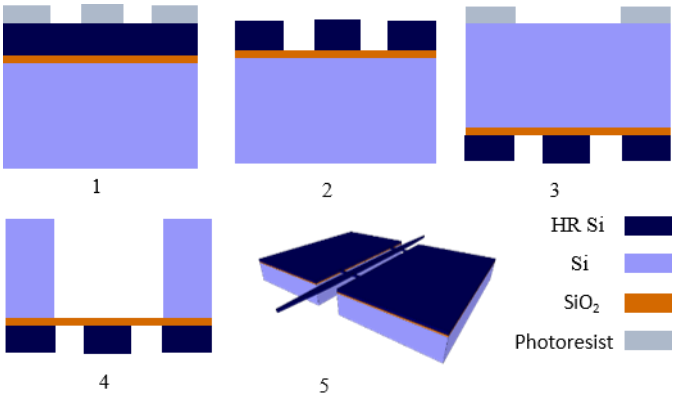

Fig. 12. Fabrication process steps

Thanks to this fabrication process, long spiral waveguide (up to 25 cm) structures with a small footprint (2x2cm), as well as different photonic crystal cavities have been fabricated and measured. The bends in these structures have a radius of 3 mm designed to present negligible radiation losses (0.02 dB/bend). Given the very high index contrast of the suspended Si guides, compact bends with radius down to 500 µm are possible (0.5 dB/bend). For space consideration the simulations of these bend losses are not shown here. In figure 13 SEM photos of the photonic crystal cavity and the suspended waveguide are shown. Note that on this scale the varying period from 106 to 120 µm is not visible.

This article has been accepted for publication in a future issue of this journal, but has not been fully edited. Content may change prior to final publication. Citation information: DOI 10.1109/TTHZ.2020.3019928, IEEE Transactions on Terahertz Science and Technology

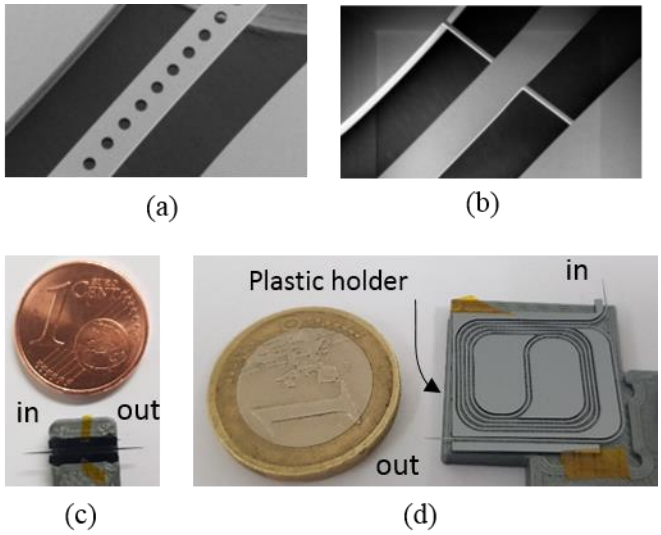

Fig. 13. Images of the fabricated samples a-b) scanning electron microscope (SEM) photo of the photonic crystal cavity (a) and the suspended waveguide (b) c-d) photographic image of the photonic crystal cavity (c) and 25 cm long waveguide (d)

VI. Experimental Measurements

The measurements of the waveguide propagation losses, and the cavities' quality factor, have been done under normal atmospheric conditions by the extraction of S parameters using a VNA (Vector Network Analyzer) with two frequency extenders and two MWG WR-1.5 ports between 500-750 GHz. The measurements are calibrated using a waveguide TRL (Thru, Reflect, Line) method, in the plane of silicon WG injection. The calibration process is repeated twice for different frequency range and frequency step. In order to measure the propagation losses and the bandgap of the photonic crystal mirrors the setup has been calibrated over the full frequency range of the extenders in steps of 125 MHz. A fine calibration (630-650 GHz with one measured point each 8 MHz frequency step) was performed for the characterization of high-Q cavity structures. In order to extract the propagation losses in the waveguide, different lengths of spiral waveguides have been fabricated (3.8, 10.9, 19.1, 25.1 cm). These structures all share the same waveguide width and thickness and same tapered sections, and only differ in total propagation length. It is important to note that these structures all share intentionally a pecular configuration for the access tapers as can be seen in fig.13.d. In order to suppress the perturbing effect of direct transmission between the WR1.5 VNA waveguide ports, the access tapers are 90° out of eachothers' axis.

Referring to section III optimal coupling is obtained by inserting the tapered section inside the MWG. This has been achieved by mounting the structures on dedicated 3D printed holders (see fig.13.c for an example) that are aligned using micropositioners and with the help of a camera to the MWG slit. The measured calibrated S_{21} and S_{11} parameters are power normalized in dB scale, representing respectively in logarithmic scale the normalized transmitted power from port 1 to port 2, and the normalized backreflected power to port 1 (Similarly for the two other parameters S_{12} and S_{22}).

$$S_{21} = 10\log_{10}\frac{I_{Transmitted}}{I_0} \quad (8)$$

$$S_{11} = 10\log_{10}\frac{I_{Reflected}}{I_0} \quad (9)$$

with I_0 the calibrated transmitted power of VNA ports. Defining,

$$T = 10^{\frac{S_{21}}{10}} \quad (10)$$

And

$$R = 10^{\frac{S_{11}}{10}} \quad (11)$$

the total losses (coupling, absorption, scattering and radiation) of the structure under test in dB scale can be obtained as

$$\boldsymbol{loss} = -\mathbf{10}\,\mathbf{log_{10}}\left(\frac{\boldsymbol{T}}{\mathbf{1-}\boldsymbol{R}}\right) \quad (12)$$

.

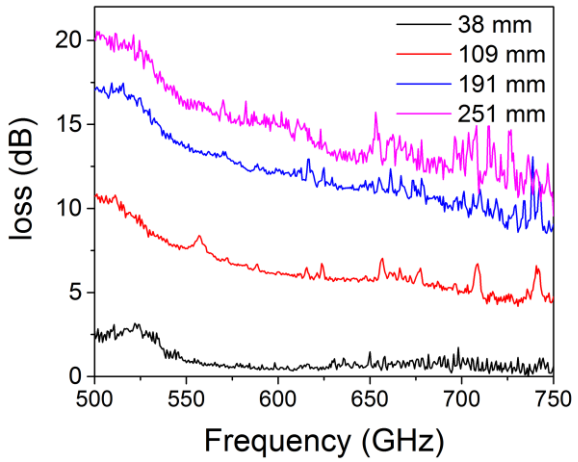

Fig. 14. Total losses for waveguides with different propagation lengths

Figure 14 represents the losses in dB for the four structures with different lengths. As expected from simulation the insertion losses are higher at low frequencies. The spectral loss behavior is similar for all measured structures. This indicates that it is safe to assume that nearly identical coupling conditions are achieved for all structures and that a plot of these losses as a function of length is meaningful. We believe the extra loss peaks appearing in some measurements to be the result of misalignments as observed in the simulations in fig.8a. A linear increase with waveguide length is observed and plotted in fig.15 for two arbitrarily chosen frequencies (600 and 700 GHz). The fitted slope α corresponds to the extracted propagation losses in dB/mm.

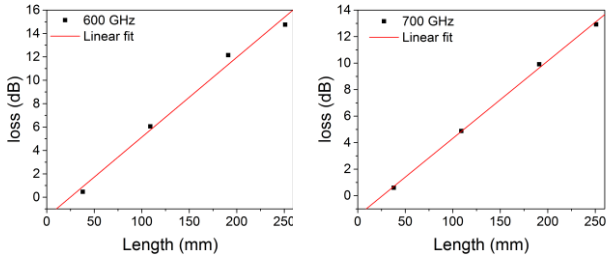

Fig. 15. Linear fit of propagation losses at 600 and 700 GHz

At 600 and 700 GHz total losses of α=0.068 and α=0.058 dB/mm respectively are observed. Note that this loss coefficient includes and distributes over the entire length of the guide all loss mechanisms (bend radiation, scattering and material absorption). It should therefore be treated as an upper limit for the pure propagation loss of the proposed suspended THz platform. This is confirmed by the fact that when extrapolating in fig.15 the linear fit to zero length in both cases would apparently lead to negative total losses. Figure 16 shows the extracted loss coefficient over the entire frequency range 500-750GHz of the extender as obtained using the above procedure. It can be stated that this novel integrated THz waveguide platform based on suspended HR-Si dielectric wire waveguides, exhibits propagation losses that vary between 0.045 and 0.085 dB/mm with an average of 0.065 dB/mm. This average loss is equivalent to 0.032 dB/λ_0. Such a value is the lowest among several other THz silicon waveguides[8]–[11]. For the first time over a large frequency band (250 GHz) extending up to 750 GHz, a very low propagation loss (including bend, material and scattering loss) is demonstrated.

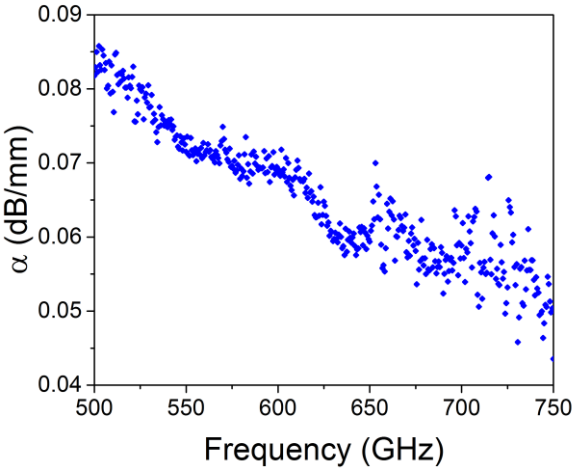

Fig. 16. Extracted propagation loss in the suspended waveguide structure

In the second part of this work we used the same measurement setup used for loss extraction to characterize the photonic crystal resonators and photonic crystal Bragg mirrors. For Bragg mirrors full band calibration is used in order to visualize the full band gap, while for the resonators a finer calibration on a limited bandwidth (630-650GHz) is used in order to resolve potential high Q resonances. Two PhC Bragg mirrors with 60 holes of 29 µm radius have been characterized: one with a period a=106.56 µm correspond to the starting period of the anodized cavity, and a second one with a=120.65 µm corresponding to its central period. Figure 17 plots the measured transmittance and reflectivity on these. In both configurations the band gap is convincingly observed, as the region of combined low S_{21} transmittance (-30dB down to -50dB) and high S_{11} reflectivity (up to -0.5dB or 90% power reflection). For the former Bragg mirror (a=106.56µm) we observe a band gap from 566 to 675.4GHz, while for the latter (a=120.65µm) the gap appears from 518.4 to 616.4GHz. Referring to the band structure simulation of fig.10, these observed band edge frequencies are in very close agreement with the numerical predictions. It is also be observed that within the allowed bands a reasonable -2dB S_{21} transmittance is observed, implying only 63% power transfer, while the S_{11} reflections back to the VNA port are still non negligible as 10-30% (-5 to -10 dB). This is to be understood as the result of the impedance mismatch at the transition between the unpatterned suspended wire guides and the etched PhC part in the suspended guide. Together with the extra small scatter losses induced by the etched holes, this also accounts for the remaining scatter losses of about 10-25%.

We also observe a "gap" at higher frequencies for both structures. These gaps do not correspond to a PhC band gap but occur when the incoming waveguide mode is coupled to higher order guided and radiative Bloch modes in the region of Brillouin zone far away from the edge. Such higher order modes are not coupled back to the monomode VNA ports, leading to a "measurement gap".

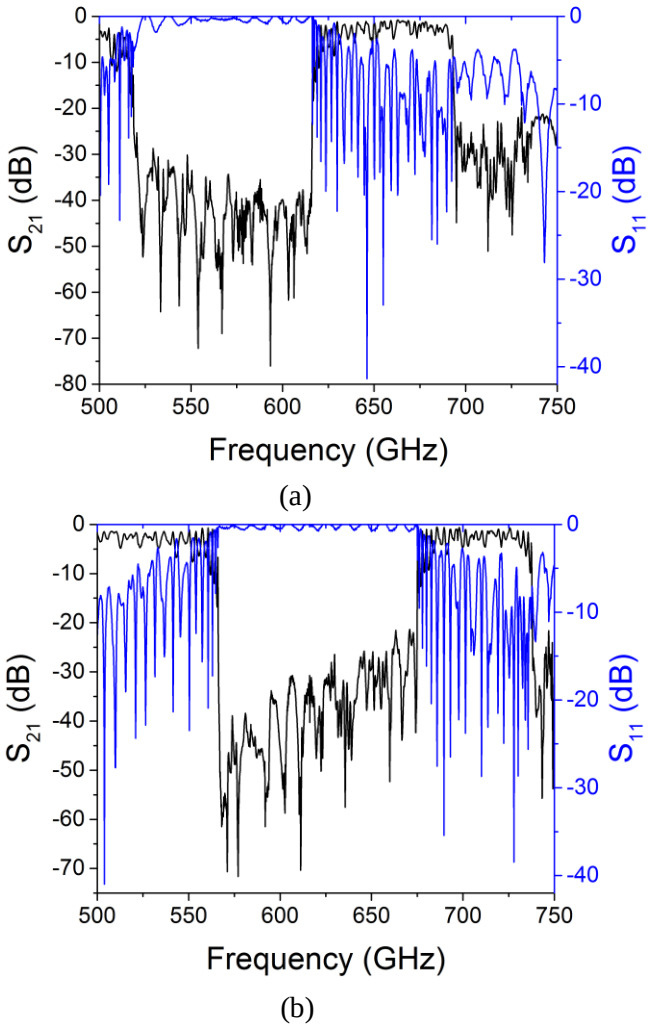

Fig. 17. Measured bandgap of photonic crystal cavities with period a) a=120.65 µm and b) a=106.56 µm

With the low-loss platform confirmed as well as the correct behavior of 1D PhC wire waveguides, the final characterization experiments consist in verifying the existence of high-Q apodized 1D PhC cavities. As described in the cavity design

section III, cavities with 3 different hole numbers are measured. For Q factor calculation we used $Q = \frac{f_R}{FWHM}$, with f_R the resonant frequency and $FWHM$ the resonance width at 3dB. In fig.18 an ultra-high $Q_{\text{measured}} = \frac{640.25}{0.034} = 1.88 \times 10^4$ is observed for the structure with N=25 holes, at 640.25 GHz. The resonant frequency is slightly blue shifted with respect to the design frequency of 636 GHz but this can be explained by a systematic fabrication shift. Indeed, SEM observation revealed a hole radius 29.4 µm, shifted by 1.3% with respect to the design radius of 29 µm.

Despite the very low losses of HR-Si, their impact on the measured quality factor is not negligible. Thus, we can extract a first order upper estimation for the intrinsic material losses out of the observed Q-factor. Indeed, the observed experimental Q-factor can be considered as the result of the idealized simulated $Q_{\text{simulated}} = 5.7 \times 10^4$ (where material losses have been neglected) and the contribution of the material losses. Using these values in the equation below

$$1/Q_{\text{Measured}} = 1/Q_{\text{simulated}} + 1/Q_{\text{Material}} \quad (13)$$

we can extract the material absorption losses as $1/Q_{Material} = 3.6\text{x}10^{-5}$ or $Q_{Material} = 2.8 \times 10^4$. The simulated results represented in IV, shows that an $\alpha = 8 \times 10^{-3}$ cm^{-1}, correspond to $Q_{\text{Material}} = 6.7 \times 10^4$ equivalent to $\tau = \frac{2Q}{\omega_0} = 3.4 \times 10^{-8}\ s$. So by analogy the experimental extracted $Q_{\text{mat}} = 2.8 \times 10^4$ corresponds to $\tau = 1.4 \times 10^{-8}\ s$ and $\alpha = 1.9 \times 10^{-2}$ cm^{-1}. Resimulating the cavity using these extracted values a total $Q = 1.83 \times 10^4$ is obtained in a 3D FDTD simulation using $\kappa_{Si} = \frac{\alpha\lambda_0}{4\pi} = 7\text{ x }10^{-5}$ as material absorption coefficient. This Q-factor of 1.83×10^4 is nearly equivalent to the measured one of 1.88×10^4, confirming the extracted material loss $\alpha = 1.9 \times 10^{-2}$ cm^{-1}. Moreover, the extracted value is very close to the one reported in [12], [13]. The very low transmission of this resonant mode (less than 1%) in this case is the result of two phenomena. First of all, the mirror reflection is very high (N=25), which is also a reason to have a high Q factor. A non-optimized injection might also account for lower overall transmission.

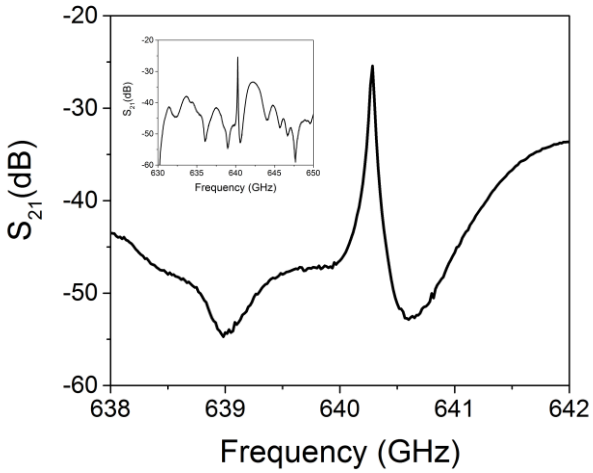

Fig. 18. Resonance frequency at f_R =640.2 GHz for cavity with N=25 hole. Inset: Zoom out of resonance plot

Such a demonstration of an ultra-high Q is very important for certain applications, while for others a combination of reasonable high Q and high transmission is necessary. This could be achieved by having less holes in the design. In a subsequent recalibrated fabrication run new cavities with less holes were produced with specific attention to compensate for the systematic deviation on the hole radius. As represented in figure 19 for the design with 21 and 17 holes respectively, the resonant frequency is closer to the one in simulation. As expected the Lorentzian peak of these resonant modes is wider than the previous one. The quality factor is decreasing from 1.88×10^4 for N=25 to 7×10^3 and 1.5×10^3 respectively for cavities with N=21 and 17. A small error still exists (less than 0.4%) on the resonance position and the resonant frequency is red shifted.

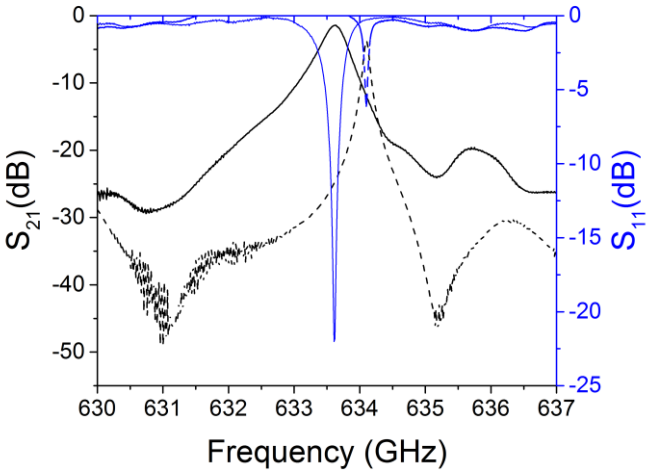

Fig. 19. Resonance frequencies at f_R = 634.1 and 633.63 GHz, for cavities with N=21 (dashed lines) and 17 (solid lines) hole respectively

However, the transmission is increasing, to reach up to 72% of transmittance (-1.4 dB) for N=17, while the mode is almost not reflected with less than 1% of reflectance (-22 dB). Similarly, for the cavity with 21 holes, S_{21}=-3.7 dB (42%) and S_{11}=-6.2 dB (24%).

To summarize, we demonstrate experimentally an ultra-high Q factor cavity, with a precise resonant frequency (error less than 0.5%) and a controllable transmittance by a simple adjustment of the number of mirror holes. These record Q factors at THz frequencies are among the highest ever reported.

VII. Conclusion

A low loss suspended Silicon platform is designed, fabricated and measured experimentally. Such an integrated platform, with a very low cost fabrication process presents very low loss. The measured propagation loss of a long waveguide with bends on a compact surface are very low α=0.065 dB/mm at f=650 GHz. Such low loss platform is also demonstrated through the design of ultra-high Q photonic crystal cavity. A Q>18000 for air confined PhC cavities at THz frequencies is measured for the first time. Other cavity design with high Q >1500 and high transmittance power >72% is also presented experimentally in this work. This novel integrated THz waveguide platform opens up new avenues for integrated sensing but may also find

interesting applications as building block for integrated THz signal processing in e.g. communication platforms.

VIII. Acknowledgement

This study was undertaken as part of the Terafood project, which is financially supported by the European Regional Development Fund and the province Oost-Vlaanderen (INTERREG V FR-WA-VL 1.1.11). The authors would like to thank S. Eliet, V. Avramovic, S. Lepilliet and E. Okada the engineers of IEMN characterization center for their assistance with the experimental measurements. They would also like to thank JM Droulez, R. Peretti, C. Tannoury and T. Hannotte for their advice on numerical calculations and computer cluster use.

IX. References

[1] P. H. Siegel, « Terahertz technology in biology and medicine », *IEEE Transactions on Microwave Theory and Techniques*, vol. 52, nº 10, p. 2438‑2447, oct. 2004, doi: 10.1109/TMTT.2004.835916.

[2] N. Laman, S. S. Harsha, D. Grischkowsky, et J. S. Melinger, « High-Resolution Waveguide THz Spectroscopy of Biological Molecules », *Biophysical Journal*, vol. 94, nº 3, p. 1010‑1020, feb. 2008, doi: 10.1529/biophysj.107.113647.

[3] J. B. Baxter et G. W. Guglietta, « Terahertz Spectroscopy », *Anal. Chem.*, vol. 83, nº 12, p. 4342‑4368, june 2011, doi: 10.1021/ac200907z.

[4] F. Hindle *et al.*, « Monitoring of food spoilage by high resolution THz analysis », *Analyst*, vol. 143, nº 22, p. 5536‑5544, nov. 2018, doi: 10.1039/C8AN01180J.

[5] K. M. K. H. Leong *et al.*, « WR1.5 Silicon Micromachined Waveguide Components and Active Circuit Integration Methodology », *IEEE Transactions on Microwave Theory and Techniques*, vol. 60, nº 4, p. 998‑1005, april 2012, doi: 10.1109/TMTT.2012.2184296.

[6] J. Hu, S. Xie, et Y. Zhang, « Micromachined Terahertz Rectangular Waveguide Bandpass Filter on Silicon-Substrate », *IEEE Microwave and Wireless Components Letters*, vol. 22, nº 12, p. 636‑638, dec. 2012, doi: 10.1109/LMWC.2012.2228179.

[7] W. H. Chow, A. Champion, et D. P. Steenson, « Measurements to 320 GHz of millimetre-wave waveguide components made by high precision and economic micro-machining techniques », in *2003 High Frequency Postgraduate Student Colloquium (Cat. No.03TH8707)*, sept. 2003, p. 90‑93, doi: 10.1109/HFPSC.2003.1242314.

[8] N. Ranjkesh, M. Basha, A. Taeb, A. Zandieh, S. Gigoyan, et S. Safavi-Naeini, « Silicon-on-Glass Dielectric Waveguide—Part I: For Millimeter-Wave Integrated Circuits », *IEEE Transactions on Terahertz Science and Technology*, vol. 5, nº 2, p. 268‑279, march 2015, doi: 10.1109/TTHZ.2015.2399693.

[9] N. Ranjkesh, M. Basha, A. Taeb, et S. Safavi-Naeini, « Silicon-on-Glass Dielectric Waveguide—Part II: For THz Applications », *IEEE Transactions on Terahertz Science and Technology*, vol. 5, nº 2, p. 280‑287, march 2015, doi: 10.1109/TTHZ.2015.2397279.

[10] H. Amarloo et S. Safavi-Naeini, « Terahertz Line Defect Waveguide Based on Silicon-on-Glass Technology », *IEEE Transactions on Terahertz Science and Technology*, vol. 7, nº 4, p. 433‑439, july 2017, doi: 10.1109/TTHZ.2017.2708505.

[11] K. Tsuruda, M. Fujita, et T. Nagatsuma, « Extremely low-loss terahertz waveguide based on silicon photonic-crystal slab », *Opt. Express, OE*, vol. 23, nº 25, p. 31977‑31990, dec. 2015, doi: 10.1364/OE.23.031977.

[12] J. Dai, J. Zhang, W. Zhang, et D. Grischkowsky, « Terahertz time-domain spectroscopy characterization of the far-infrared absorption and index of refraction of high-resistivity, float-zone silicon », *J. Opt. Soc. Am. B, JOSAB*, vol. 21, nº 7, p. 1379‑1386, july 2004, doi: 10.1364/JOSAB.21.001379.

[13] D. Grischkowsky, S. Keiding, M. van Exter, et C. Fattinger, « Far-infrared time-domain spectroscopy with terahertz beams of dielectrics and semiconductors », *J. Opt. Soc. Am. B, JOSAB*, vol. 7, nº 10, p. 2006‑2015, oct. 1990, doi: 10.1364/JOSAB.7.002006.

[14] M. Naftaly et R. E. Miles, « Terahertz Beam Interactions with Amorphous Materials », in *Terahertz Frequency Detection and Identification of Materials and Objects*, Dordrecht, 2007, p. 107‑122.

[15] K. Tsuruda, M. Fujita, et T. Nagatsuma, « Extremely low-loss terahertz waveguide based on silicon photonic-crystal slab », *Opt. Express, OE*, vol. 23, nº 25, p. 31977‑31990, dec. 2015, doi: 10.1364/OE.23.031977.

[16] P. B. Deotare, M. W. McCutcheon, I. W. Frank, M. Khan, et M. Lončar, « High quality factor photonic crystal nanobeam cavities », *Appl. Phys. Lett.*, vol. 94, nº 12, p. 121106, march 2009, doi: 10.1063/1.3107263.

[17] Y. Akahane, T. Asano, B.-S. Song, et S. Noda, « High-Q photonic nanocavity in a two-dimensional photonic crystal », *Nature*, vol. 425, nº 6961, p. 944‑947, oct. 2003, doi: 10.1038/nature02063.

[18] W. Xie *et al.*, « High-Q Photonic Crystal Nanocavities on 300 mm SOI Substrate Fabricated With 193 nm Immersion Lithography », *J. Lightwave Technol., JLT*, vol. 32, nº 8, p. 1457‑1462, april 2014.

[19] D. Yang, X. Chen, X. Zhang, C. Lan, et Y. Zhang, « High-Q, low-index-contrast photonic crystal nanofiber cavity for high sensitivity refractive index sensing », *Appl. Opt., AO*, vol. 57, nº 24, p. 6958‑6965, august 2018, doi: 10.1364/AO.57.006958.

[20] P. Lalanne, C. Sauvan, et J. P. Hugonin, « Photon confinement in photonic crystal nanocavities », *Laser & Photonics Reviews*, vol. 2, nº 6, p. 514‑526, 2008, doi: 10.1002/lpor.200810018.

[21] Q. Quan, P. B. Deotare, et M. Loncar, « Photonic crystal nanobeam cavity strongly coupled to the feeding waveguide », *Appl. Phys. Lett.*, vol. 96, nº 20, p. 203102, may 2010, doi: 10.1063/1.3429125.

[22] D. Yang, C. Wang, et Y. Ji, « Silicon on-chip 1D photonic crystal nanobeam bandstop filters for the parallel multiplexing of ultra-compact integrated sensor array », *Opt. Express, OE*, vol. 24, nº 15, p. 16267-16279, july 2016, doi: 10.1364/OE.24.016267.

[23] E. Kuramochi, H. Taniyama, T. Tanabe, K. Kawasaki, Y.-G. Roh, et M. Notomi, « Ultrahigh-Q one-dimensional photonic crystal nanocavities with modulated mode-gap barriers on SiO_2 claddings and on air claddings », *Opt. Express, OE*, vol. 18, nº 15, p. 15859 -15869, july 2010, doi: 10.1364/OE.18.015859.

[24] S. M. Hanham, M. M. Ahmad, S. Lucyszyn, et N. Klein, « LED-Switchable High-Q Packaged THz Microbeam Resonators », *IEEE Transactions on Terahertz Science and Technology*, vol. 7, nº 2, p. 199-208, mars 2017, doi: 10.1109/TTHZ.2016.2634547.

[25] A. L. Bingham et D. Grischkowsky, « Terahertz two-dimensional high-Q photonic crystal waveguide cavities », *Optics Letters*, vol. 33, nº 4, p. 348, feb. 2008, doi: 10.1364/OL.33.000348.

[26] Y. Miyamoto, H. Kanaoka, et S. Kirihara, « Terahertz wave localization at a three-dimensional ceramic fractal cavity in photonic crystals », *Journal of Applied Physics*, vol. 103, nº 10, p. 103106, may 2008, doi: 10.1063/1.2924327.

[27] J. Xie, X. Zhu, X. Zang, Q. Cheng, L. Chen, et Y. Zhu, « Terahertz integrated device: high-Q silicon dielectric resonators », *Optical Materials Express*, vol. 8, nº 1, p. 50, jan. 2018, doi: 10.1364/OME.8.000050.

[28] C. M. Yee et M. S. Sherwin, « High-Q terahertz microcavities in silicon photonic crystal slabs », *Applied Physics Letters*, vol. 94, nº 15, p. 154104, april 2009, doi: 10.1063/1.3118579.

[29] W. J. Otter, S. M. Hanham, N. M. Ridler, G. Marino, N. Klein, et S. Lucyszyn, « 100GHz ultra-high Q-factor photonic crystal resonators », *Sensors and Actuators A: Physical*, vol. 217, p. 151-159, sept. 2014, doi: 10.1016/j.sna.2014.06.022.

[30] K. Okamoto, K. Tsuruda, S. Diebold, S. Hisatake, M. Fujita, et T. Nagatsuma, « Terahertz Sensor Using Photonic Crystal Cavity and Resonant Tunneling Diodes », *J Infrared Milli Terahz Waves*, vol. 38, nº 9, p. 1085-1097, sept. 2017, doi: 10.1007/s10762-017-0391-0.

[31] S. M. Hanham, C. Watts, W. J. Otter, S. Lucyszyn, et N. Klein, « Dielectric measurements of nanoliter liquids with a photonic crystal resonator at terahertz frequencies », *Appl. Phys. Lett.*, vol. 107, nº 3, p. 032903, july 2015, doi: 10.1063/1.4927242.

[32] Yasuo KOKUBUN, « High index contrast optical waveguides and their applications to microring filter circuit wavelength selective switch », *IEICE Trans. Electron*, vol. E90-C, nº 5, may 2007.

[33] « High-Performance Photonic Simulation Software », *Lumerical*. https://www.lumerical.com/.

[34] E. Akiki *et al.*, « Terahertz photoacoustic gas sensor », Saint Raphaël, France, june 2019.

[35] M. Verstuyft, E. Akiki, B. Walter, M. Faucher, M. Vanwolleghem, et B. Kuyken, « An Integrated Photoacoustic Terahertz Gas Sensor », in *2019 44th International Conference on Infrared, Millimeter, and Terahertz Waves (IRMMW-THz)*, sept. 2019, p. 1-2, doi: 10.1109/IRMMW-THz.2019.8873764.

[36] M. Verstuyft *et al.*, « Proposal for an integrated silicon-photonics terahertz gas detector using photoacoustics », *Optics Express*, july 2020, doi: 10.1364/OE.397272.

[37] G. E. Ponchak, N. I. Dib, et L. P. B. Katehi, « Design and analysis of transitions from rectangular waveguide to layered ridge dielectric waveguide », *IEEE Transactions on Microwave Theory and Techniques*, vol. 44, nº 7, p. 1032-1040, july 1996, doi: 10.1109/22.508635.

[38] J. D. Love, W. M. Henry, W. J. Stewart, R. J. Black, S. Lacroix, et F. Gonthier, « Tapered single-mode fibres and devices. I. Adiabaticity criteria », *IEE Proceedings J - Optoelectronics*, vol. 138, nº 5, p. 343-354, oct. 1991, doi: 10.1049/ip-j.1991.0060.

[39] E. Kuramochi, H. Taniyama, T. Tanabe, K. Kawasaki, Y.-G. Roh, et M. Notomi, « Ultrahigh-Q one-dimensional photonic crystal nanocavities with modulated mode-gap barriers on SiO_2 claddings and on air claddings », *Opt. Express, OE*, vol. 18, nº 15, p. 15859 -15869, july 2010, doi: 10.1364/OE.18.015859.

[40] Q. Quan et M. Loncar, « Deterministic design of wavelength scale, ultra-high Q photonic crystal nanobeam cavities », *Optics Express*, vol. 19, nº 19, p. 18529, sept. 2011, doi: 10.1364/OE.19.018529.

[41] « COMSOL: Multiphysics Software for Optimizing Designs », *COMSOL Multiphysics®*. https://www.comsol.fr/.

[42] J. D. Joannopoulos, Éd., *Photonic crystals: molding the flow of light*, 2nd ed. Princeton: Princeton University Press, 2008.

[43] « US5501893A - Method of anisotropically etching silicon - Google Patents ». https://patents.google.com/patent/US5501893A/en